

In Situ Observed Local Structural Distortions Boost Solar Water Splitting in Hematite

Cheng Lu,^{||} Zihou Jiang,^{||} Jiabin Xu, Shuo Li, Yong Feng, Bai Xu, Gongcheng Liu, Ye Zhu, Kun Feng, and Jun Zhong*



Cite This: *ACS Catal.* 2025, 15, 18416–18425



Read Online

ACCESS |

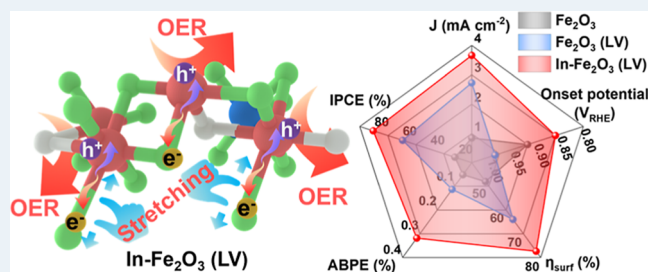
Metrics & More

Article Recommendations

Supporting Information

ABSTRACT: Although hematite ($\alpha\text{-Fe}_2\text{O}_3$) is considered a promising photoanode material for photoelectrochemical (PEC) water splitting, its practical application is limited by inherently low charge transport efficiency and sluggish oxygen evolution reaction (OER) kinetics. In this study, in situ synchrotron X-ray absorption spectroscopy (XAS) was employed under illumination to distinctly observe the transient electronic structure changes at Fe sites and to elucidate their structure–activity relationship with the stretching of Fe–O bond. It is revealed that local distortions induced by Fe–O bond stretching enhance the hybridization of O 2p–Fe 3d orbitals, promote electron transfer, and facilitate the formation of Fe^{4+} active sites. Such structural modulation significantly suppresses surface charge recombination, thus accelerating the OER kinetics. Leveraging this mechanism, an In- Fe_2O_3 (LV) photoanode was constructed, delivering a photocurrent density of 3.66 mA cm^{-2} at $1.23 V_{\text{RHE}}$, with an onset potential negatively shifted to $0.86 V_{\text{RHE}}$. Upon coupling with a FeNiOOH cocatalyst, the photocurrent density is further enhanced to 4.32 mA cm^{-2} , and the onset potential is reduced to $0.77 V_{\text{RHE}}$. This study employs atomic-scale in situ characterization to systematically elucidate the structure–activity relationship between local lattice distortions and enhanced OER performance, providing actionable insights and strategies for the rational design of high-efficiency photoanodes.

KEYWORDS: hematite, oxygen vacancies, in situ XAS, solar water splitting, Fe–O bond stretching



INTRODUCTION

Harnessing the earth's abundant solar energy and water resources for photoelectrochemical (PEC) water splitting to produce green hydrogen is regarded as a promising strategy to address the challenges of energy shortages and environmental pollution.^{1–4} Among the various reported photoanode materials, hematite ($\alpha\text{-Fe}_2\text{O}_3$) has attracted considerable attention due to its suitable band gap ($\sim 2.1 \text{ eV}$), earth abundance, low cost, and excellent corrosion resistance.^{5–7} However, the practical performance of hematite photoanodes remains significantly limited by severe charge recombination, intrinsically low conductivity, and sluggish oxygen evolution reaction (OER) kinetics, falling far short of the theoretical solar-to-hydrogen (STH) conversion efficiency.^{8–10} To overcome these intrinsic limitations and enhance the catalytic performance of hematite photoanodes, a range of modification strategies have been developed, including morphology engineering, elemental doping, surface passivation, heterojunction construction, and cocatalyst integration.¹¹

Elemental doping has emerged as an effective strategy to enhance the PEC performance of hematite, enabling modulation of the band structure and the introduction of structural distortions by incorporating various impurity ions (such as Ti,^{12–15} Sn,^{16–19} Ta,^{8,20} Zr^{21,22}) or oxygen

vacancies.^{23,24} These modifications can increase the conductivity of the photoanode and suppress charge carrier recombination. For example, single-atom Pt doping, as reported by Wang et al., significantly prolonged the charge transfer lifetime within the bulk of hematite and improved carrier injection efficiency at the semiconductor/electrolyte interface.²⁵ Moreover, the combined approach of morphology engineering (porous nanorods) and multielement codoping (Ge, Ti, Sn), demonstrated by Jang et al., effectively addressed the challenges of intrinsically low conductivity and short hole diffusion lengths in hematite.²⁶ However, nonuniform spatial distribution of dopants and the accumulation of lattice strain during the doping process often result in a trade-off between carrier mobility and lattice distortion, which imposes significant limitations on achieving ideal carrier transport efficiency.

Received: July 14, 2025

Revised: October 15, 2025

Accepted: October 16, 2025

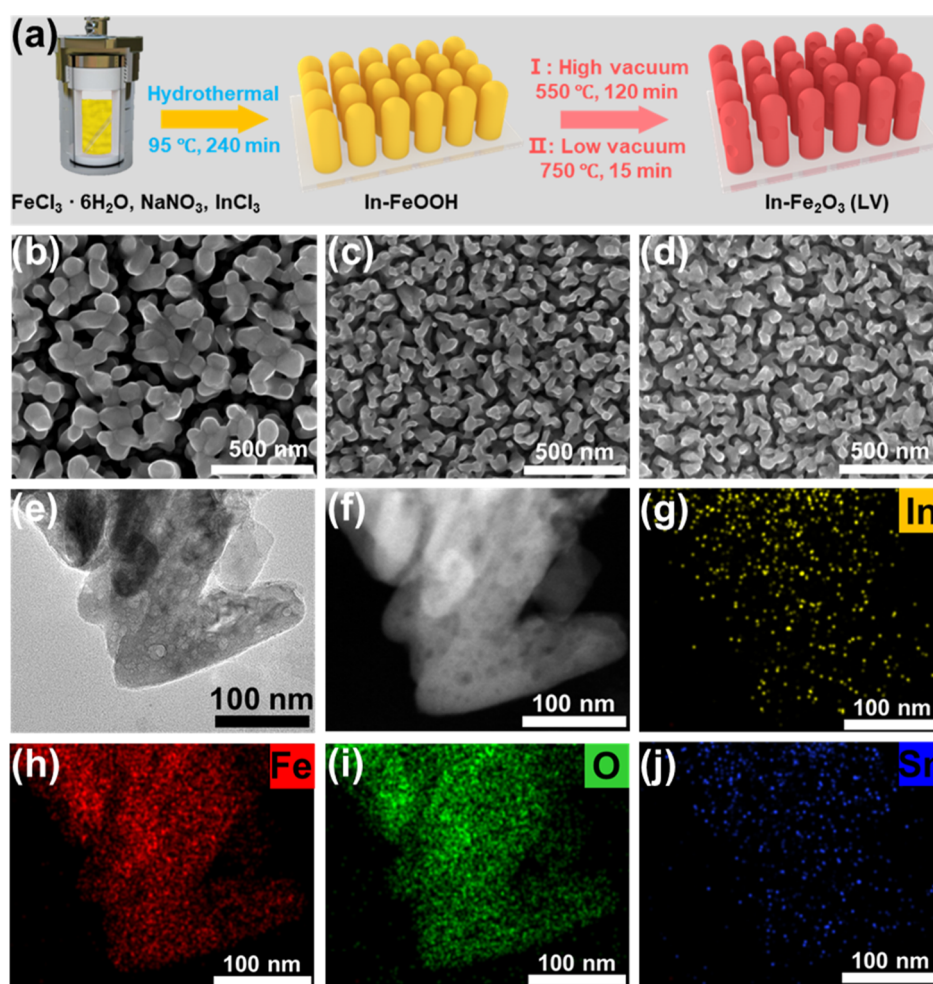


Figure 1. Synthesis procedure and morphology. (a) Illustration for the synthesis of In-Fe₂O₃ (LV). (b–d) Top view SEM images of (b) Fe₂O₃, (c) Fe₂O₃ (LV) and (d) In-Fe₂O₃ (LV), respectively. (e) TEM images and (f–j) elemental mappings of In-Fe₂O₃ (LV).

In pursuit of advanced photoanode performance, considerable attention has been devoted to elucidating the interfacial charge transfer mechanisms in photoanode materials. For instance, Zhang et al. have demonstrated the modulatory effect of Ni_{1–2}Fe_xOOH on proton-coupled electron transfer (PCET) processes during water oxidation across various typical photoanodes.²⁷ Durrant's group has shown that, owing to an equilibrium between surface holes and M(OH)–O–M(OH) active sites, hematite can facilitate water oxidation via a pathway with reduced activation energy.²⁸ Li et al. have identified key reaction intermediates in the OER process on hematite and highlighted the potential impact of O₂ desorption on overall reaction kinetics.²⁹ These mechanistic insights have provided valuable guidance for the rational design of hematite-based photoanodes. However, the atomic-scale, dynamic understanding of bulk charge transport and interfacial reaction mechanisms in hematite—such as changes in bond length, orbital hybridization, and unoccupied electronic states—remains limited. This lack of in-depth knowledge blurs the connection between the design of advanced catalysts and fundamental reaction mechanisms, thus significantly hindering further breakthroughs in the photogenerated current density of hematite photoanodes.

In this work, a synergistic strategy combining indium (In) doping with oxygen vacancies (along with heterophase) was employed to construct In-Fe₂O₃ (LV) photoanodes featuring

deliberate local structural distortions. Atomic-scale transient changes at Fe sites were observed by in situ X-ray absorption spectroscopy (XAS), and the regulatory mechanism by which Fe–O bond stretch-induced local structural distortion influences the OER performance of hematite was systematically elucidated. The stretching of the Fe–O bond enhances O 2p-Fe 3d orbital hybridization, thereby significantly promoting electron transfer and mitigating the adverse impact of lattice stress on charge transport. Furthermore, such a distorted structure facilitates the formation of Fe⁴⁺ active sites, accelerating surface charge separation, and thereby markedly improving the OER kinetics. The In-Fe₂O₃ (LV) photoanode achieves a photocurrent density of 3.66 mA cm^{–2} at 1.23 V_{RHE} and an onset potential of 0.86 V_{RHE}; upon coupling with a FeNiOOH cocatalyst (FeNiOOH–In-Fe₂O₃ (LV)), performance is further enhanced to 4.32 mA cm^{–2} with an onset potential of 0.77 V_{RHE}, ranking among the highest values reported for hematite photoanodes. These findings not only deepen the fundamental understanding of the influence of local structural modulation on the OER mechanism of hematite, but also provide valuable guidance for the rational design of high-performance photoanodes for water splitting.

RESULTS AND DISCUSSION

Synthesis and Characterization. FeOOH and In-FeOOH nanorod arrays were first synthesized on FTO

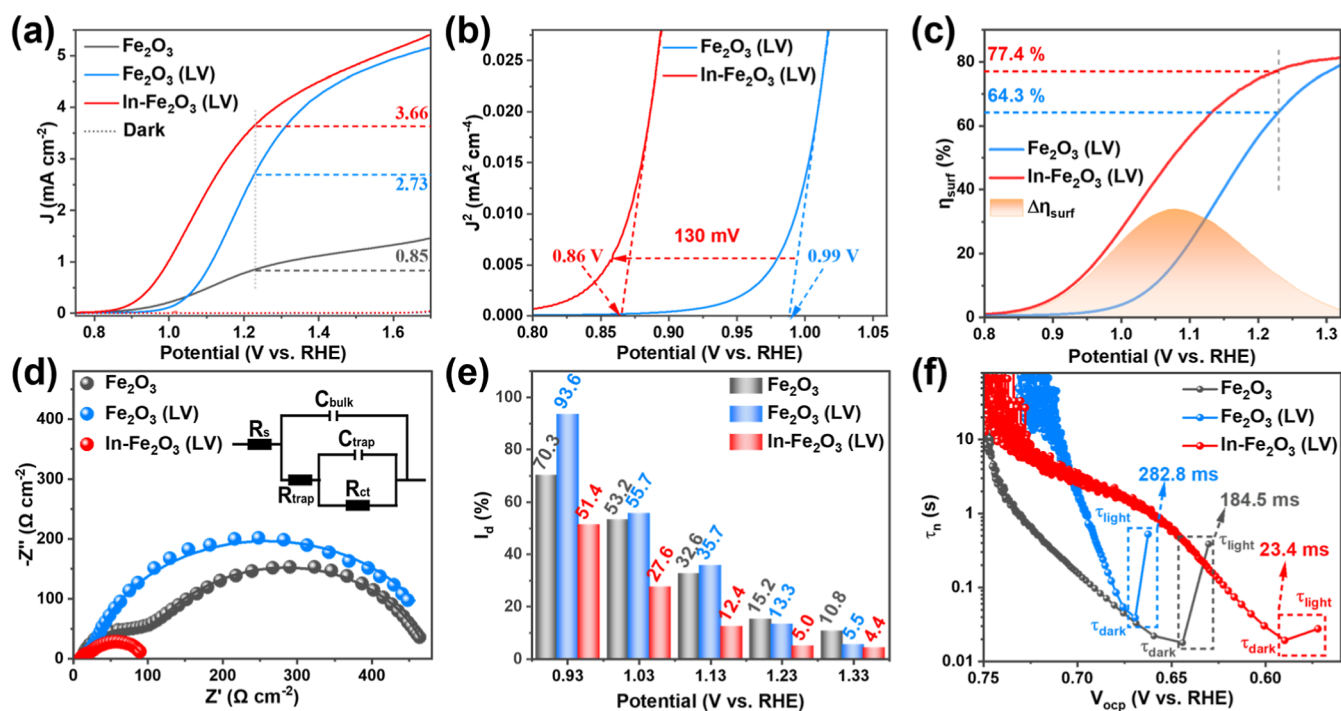


Figure 2. Electrochemical performance and analysis of In-Fe₂O₃ (LV), Fe₂O₃ (LV) and Fe₂O₃. (a) *J*–*V* curves of In-Fe₂O₃ (LV), Fe₂O₃ (LV) and Fe₂O₃. (b) Enlarged *J*²–*V* curves of In-Fe₂O₃ (LV) and Fe₂O₃ (LV). (c) Surface charge separation efficiencies (η_{surf}) and $\Delta\eta_{\text{surf}}$ of In-Fe₂O₃ (LV) and Fe₂O₃ (LV). (d) PEIS spectra, (e) *I*_d (at 0.93, 1.03, 1.13, 1.23, and 1.33 V_{RHE}) and (f) OCP-derived carrier lifetimes of In-Fe₂O₃ (LV), Fe₂O₃ (LV) and Fe₂O₃.

conductive glass substrates via a conventional hydrothermal approach. Subsequently, a custom-designed two-step high-temperature annealing process under variable pressure was employed to introduce oxygen vacancies (along with heterophase) into the hematite, yielding the modified photoanodes denoted as Fe₂O₃ (LV) (Figure S1) and In-Fe₂O₃ (LV) (Figure 1a), respectively.^{30,31} For comparison, pristine α -Fe₂O₃ (Fe₂O₃) (Figure S1) and indium-doped α -Fe₂O₃ (In-Fe₂O₃) (Figure S2) were prepared using a standard annealing procedure.

X-ray diffraction (XRD) was employed to investigate the phase composition and crystalline structure of the modified photoanodes. As shown in Figure S3, all samples exhibit diffraction peaks that can be indexed to α -Fe₂O₃, with the (110) plane as the predominant orientation, confirming the successful synthesis of the hematite phase.³² Additional diffraction peaks originate from SnO₂ in the FTO substrate.³³ Due to the low doping concentration, no distinct peaks attributable to indium species are observed in In-Fe₂O₃ (LV). As shown in the magnified part of Figure S3, in addition to α -Fe₂O₃ as the primary phase and SnO₂ from the FTO substrate, a diffraction peak at $2\theta = 33^\circ$ can also be observed in both Fe₂O₃ (LV) and In-Fe₂O₃ (LV). This peak can be attributed to the formation of β -Fe₂O₃ (PDF #39-0238).

Scanning electron microscopy (SEM) and transmission electron microscopy (TEM) were further utilized to examine the morphology and microstructure of the samples.³⁴ SEM images (Figure 1b, c and d) reveal that the nanorods in Fe₂O₃ (LV) and In-Fe₂O₃ (LV) exhibit significantly reduced dimensions compared to those of pristine Fe₂O₃. TEM images (Figure 1e) further demonstrate the presence of a porous nanorod architecture. Moreover, as shown in Figure S4a, pristine Fe₂O₃ exhibits a Brunauer–Emmett–Teller (BET)

value of 3.9630 m² g⁻¹, which is much lower than that of Fe₂O₃ (LV) (6.8833 m² g⁻¹) and In-Fe₂O₃ (LV) (7.5286 m² g⁻¹).⁶ These results indicate that the porous structure induced by low-vacuum annealing can increase the specific surface area. The reduced size and enhanced porosity are expected to increase the specific surface area and shorten charge transport pathways, which play a crucial role in improving the catalytic performance of the photoanodes.^{7,26}

For In-Fe₂O₃ (LV), high-resolution TEM (HRTEM) images (Figure S4b) clearly show the presence of β -Fe₂O₃ and pronounced grain boundaries, providing direct evidence for the successful incorporation of heterostructures, consistent with previous reports.^{30,31} Elemental mapping (Figures 1f–j, S5 and S6) reveals a uniform distribution of Fe and O elements, along with a distinct and homogeneous indium signal, further confirming the successful introduction of indium into the photoanode.

PEC Performance for Photoanodes. The performance of In-Fe₂O₃ (LV) photoanodes was optimized by adjusting the amount of indium chloride (InCl₃) precursor, with the corresponding *J*–*V* curves presented in Figure S7. As shown in Figure 2a, both Fe₂O₃ (LV) and In-Fe₂O₃ (LV) exhibit significantly enhanced photocurrent densities of 2.73 and 3.66 mA cm⁻², respectively, at 1.23 V_{RHE}, compared to pristine Fe₂O₃ (0.85 mA cm⁻²). The PEC performance of pure β -Fe₂O₃ is relatively low.^{30,35} However, the heterophase (β -Fe₂O₃) in Fe₂O₃ (LV) gives rise to abundant interfacial structures, which are favorable to the formation of oxygen vacancies.¹³ In addition, such interfacial architectures can alleviate internal stress and, through the formation of oxygen vacancies, effectively reduce defects in the bulk (and/or at the surface). The improved performance of Fe₂O₃ (LV) can be attributed to the enhanced conductivity resulting from oxygen

vacancies and the favorable effect from the heterophase of β - Fe_2O_3 , in good agreement with previously reported values.^{22,31} Notably, the optimized In- Fe_2O_3 (LV) achieves a photocurrent density 4.3 times higher than that of pristine Fe_2O_3 , highlighting the substantial promoting effect of indium incorporation on the catalytic activity of the photoanodes. Furthermore, Figure 2b clearly illustrates the shifts in onset potential for different photoanodes.^{36,37} The In- Fe_2O_3 (LV) photoanode displays an onset potential of approximately 0.86 V_{RHE} , which is 130 mV more negative than that of Fe_2O_3 (LV) (0.99 V_{RHE}), indicating that the introduction of indium effectively mitigates the increased onset potential induced by oxygen vacancies.

Comprehensive electrochemical measurements were conducted to elucidate the origins of the enhanced performance and lowered onset potential observed in the In- Fe_2O_3 (LV) photoanode. The charge separation properties of various photoanodes during PEC water splitting were systematically investigated using H_2O_2 as a hole scavenger.^{33,38} The J - V curves for these photoanodes are presented in Figure S8. Based on established equations, the surface charge separation efficiency (η_{surf}) and bulk charge separation efficiency (η_{bulk}) were quantitatively evaluated for each sample. As illustrated in Figure 2c, the dependence of $\Delta\eta_{\text{surf}}$ on the applied potential clearly indicates a substantial enhancement of surface charge separation efficiency in In- Fe_2O_3 (LV) relative to Fe_2O_3 (LV). At 1.23 V_{RHE} , η_{surf} for In- Fe_2O_3 (LV) reaches 77.4%, which is markedly higher than the values for Fe_2O_3 (LV) (64.3%) and pristine Fe_2O_3 (48.8%, see Figure S9a). Similarly, the η_{bulk} values for different photoanodes are shown in Figures S9b and S10a. Owing to the synergistic effects of oxygen vacancies and heterophase, In- Fe_2O_3 (LV) and Fe_2O_3 (LV) exhibit substantially improved η_{bulk} values of 37.8 and 34.4%, respectively, compared to the limited value of 14.2% for Fe_2O_3 at 1.23 V_{RHE} .³⁰ The $\Delta\eta_{\text{bulk}}$ results in Figure S10a further corroborate the pronounced bulk charge separation enhancement in In- Fe_2O_3 (LV). Collectively, the comodification strategy involving indium doping and oxygen vacancies (along with heterophase) not only reinforces bulk charge separation efficiency but also significantly improves surface charge separation efficiency. As a result, the In- Fe_2O_3 (LV) photoanode achieves a high photocurrent density of 3.66 mA cm^{-2} at 1.23 V_{RHE} , with the onset potential negatively shifted by 130 mV.

Subsequently, the Mott-Schottky plots presented in Figure S11 reveal notable variations in carrier concentration (N_d) among the different photoanodes, where a smaller slope indicates a higher carrier density.^{39,40} The carrier concentration in In- Fe_2O_3 (LV) ($5.72 \times 10^{18} \text{ cm}^{-3}$) is significantly higher compared to that in pristine Fe_2O_3 ($9.29 \times 10^{17} \text{ cm}^{-3}$). The modest carrier increase of In- Fe_2O_3 (LV) when compared to Fe_2O_3 (LV) ($4.81 \times 10^{18} \text{ cm}^{-3}$) likely arises from the local structural changes caused by Fe-O bond elongation upon In incorporation.⁴¹ Furthermore, Figure 2d displays the raw and fitted data from photoelectrochemical impedance spectroscopy (PEIS) measurements, along with the equivalent circuit model used to analyze the charge transfer characteristics of the various photoanodes; associated fitting parameters are summarized in Table S1.^{42,43} Among all samples, In- Fe_2O_3 (LV) shows the smallest semicircular diameter in the Nyquist plots, indicative of the lowest bulk resistance (R_{trap}) and interfacial charge transfer resistance (R_{ct}).⁴⁴ According to the fitted impedance values in Table S1, the calculated charge

transfer efficiency (η_{trans}) values for In- Fe_2O_3 (LV), Fe_2O_3 (LV), and pristine Fe_2O_3 are 31.60, 5.94, and 23.64%, respectively.⁴⁵ Among these, In- Fe_2O_3 (LV) exhibits the highest charge transfer efficiency, whereas Fe_2O_3 (LV) shows a reduced efficiency due to the excessive surface recombination centers. Moreover, the R_{ct} value for In- Fe_2O_3 (LV) is only 58.0 Ω , substantially lower than that of Fe_2O_3 (LV) (460.7 Ω), highlighting the significant enhancement in interfacial charge transfer enabled by the combined indium incorporation and oxygen vacancies modification (along with heterophase).^{26,46} In addition, compared to Fe_2O_3 (LV), In- Fe_2O_3 (LV) shows twice the C_{trap} value, likely due to the favorable formation of high-valence Fe species.⁴⁷

In addition, photocurrent decay (I_d) values under various applied potentials were measured to further assess surface charge recombination behavior, with results summarized in Figures 2e and S12.⁴⁸ Across the potential range of 0.93–1.33 V_{RHE} , In- Fe_2O_3 (LV) consistently exhibits lower I_d values compared to Fe_2O_3 and Fe_2O_3 (LV), evidencing a pronounced suppression of surface charge recombination processes. Collectively, these findings further substantiate the superior OER performance achieved with the In- Fe_2O_3 (LV) photoanode. The transient decay profile of open-circuit potential (OCP) offers deeper insights into the dynamics of photo-generated charge carriers.^{46,49} As illustrated in Figure S13a, In- Fe_2O_3 (LV) exhibits a photovoltage ($\Delta\text{OCP} = \text{OCP}_{\text{dark}} - \text{OCP}_{\text{light}}$) of 210 mV, distinctly higher than that of Fe_2O_3 (LV) (113 mV) and pristine Fe_2O_3 (176 mV), indicating a significantly enhanced charge separation efficiency. Among them, Fe_2O_3 (LV) exhibits a smaller ΔOCP than Fe_2O_3 , which can be attributed to severe surface charge recombination on Fe_2O_3 (LV). This is consistent with the higher onset potential observed for Fe_2O_3 (LV).⁵⁰

To further elucidate the OCP-derived carrier lifetimes, the instantaneous state changes upon light-off were analyzed, as indicated by the green ellipse region in Figure S13a. The obtained results were shown in Figure 2f. The calculated OCP-derived carrier lifetime for each sample can be assigned as the average of the lifetimes at the two points with light on and off (τ_{light} and τ_{dark} labeled in Figure 2f).⁴⁵ The obtained carrier lifetime of In- Fe_2O_3 (LV) on the millisecond time scale (Figure 2f) is approximately 23.4 ms, which is markedly shorter than that of Fe_2O_3 (LV) (282.8 ms) and Fe_2O_3 (184.5 ms), indirectly reflecting more efficient charge separation under illumination.^{16,45}

The SPV spectra have been shown in Figure S13b. The spectra indicate that all the Fe_2O_3 -based electrodes exhibit positive SPV signals.⁹ Among them, In- Fe_2O_3 (LV) displays the strongest positive signal intensity when compared with Fe_2O_3 (LV) and Fe_2O_3 , indicating a markedly enhanced charge-separation capability to effectively promote the carrier separation and transfer.⁹ As shown in Figure S14a, the steady-state photoluminescence (PL) response intensity of In- Fe_2O_3 (LV) is lower than those of Fe_2O_3 (LV) and Fe_2O_3 , indicating substantial suppression of photogenerated charge recombination in the photoanode.⁴⁵ Meanwhile, the time-resolved transient photoluminescence (TRPL) spectra in Figure S14b (using a three-exponential fitting model) show that the average carrier lifetime of In- Fe_2O_3 (LV) is 8.99 ns, higher than 4.60 ns for Fe_2O_3 (LV) and 7.61 ns for Fe_2O_3 , suggesting that a larger fraction of photogenerated electrons and holes to participate in the photoelectrochemical coupling processes.⁹

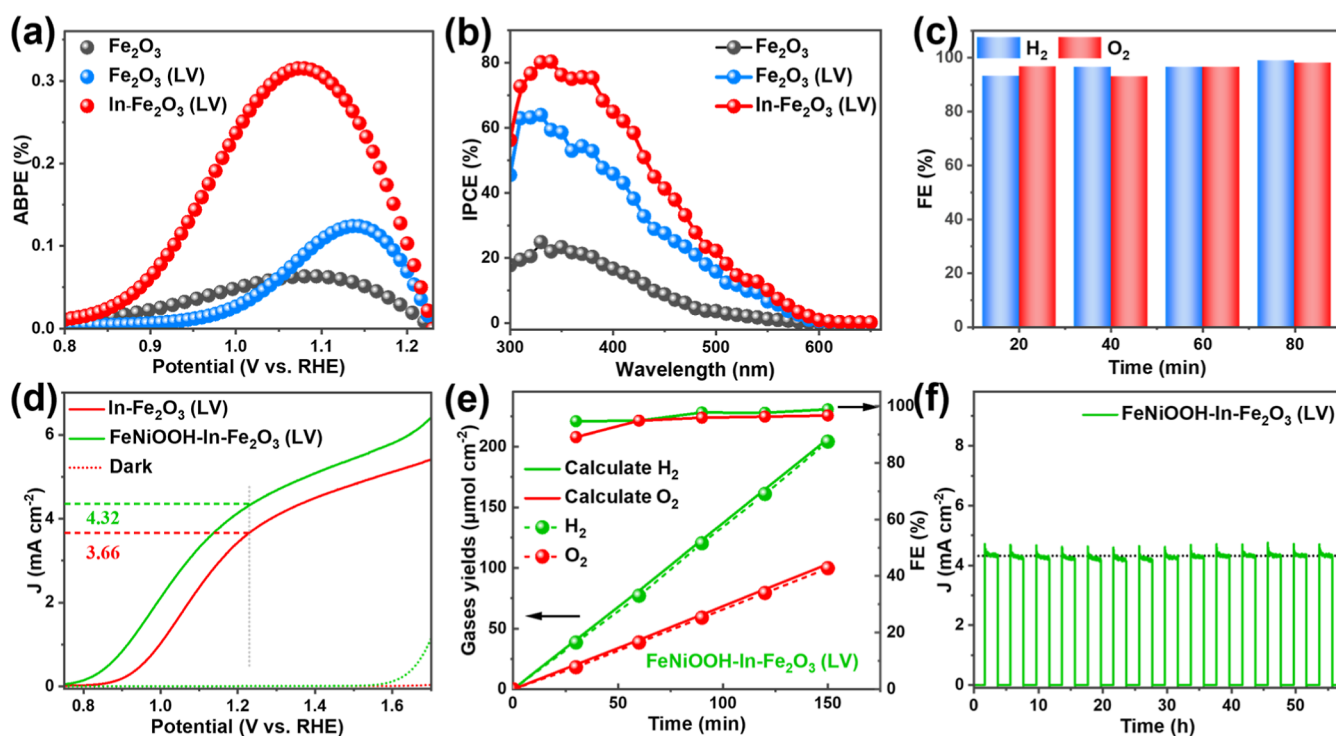


Figure 3. Electrochemical performance and characterization of In-Fe₂O₃ (LV) and FeNiOOH-In-Fe₂O₃ (LV). (a) ABPE and (b) IPCE of In-Fe₂O₃ (LV), Fe₂O₃ (LV) and Fe₂O₃. (c) The Faradaic efficiencies (FEs) of In-Fe₂O₃ (LV) with an applied bias of 1.23 V_{RHE}. (d) *J*-*V* curves of FeNiOOH-In-Fe₂O₃ (LV) and In-Fe₂O₃ (LV). (e) O₂ and H₂ evolution curves (left axis) for FeNiOOH-In-Fe₂O₃ (LV) and the corresponding FEs at 1.23 V_{RHE} (top curves, right axis). (f) *I*-*t* curve of FeNiOOH-In-Fe₂O₃ (LV) at 1.23 V_{RHE}.

Electrochemical double-layer capacitance (C_{dl}), obtained from cyclic voltammetry (CV) measurements at various scan rates (Figure S15a–c), was used to estimate the electrochemically active surface area (ECSA) of the photoanodes.^{50,51} As shown in Figure S15d, In-Fe₂O₃ (LV) exhibits an ECSA as high as 140.0 $\mu\text{F cm}^{-2}$, which is notably higher than those of Fe₂O₃ (LV) (80.1 $\mu\text{F cm}^{-2}$) and Fe₂O₃ (40.3 $\mu\text{F cm}^{-2}$). These results demonstrate that the comodification with indium and oxygen vacancies (along with heterophase) effectively increases the density of active sites on the photoanode surface.

As shown in Figure 3a, In-Fe₂O₃ (LV) exhibits the highest applied bias photon-to-current efficiency (ABPE) of 0.32%, markedly surpassing those of Fe₂O₃ (LV) (0.12%) and pristine Fe₂O₃ (0.06%).^{52,53} In addition, In-Fe₂O₃ (LV) demonstrates a maximum incident photon-to-current efficiency (IPCE) of 80.4% at 350 nm under 1.23 V_{RHE} (Figure 3b), significantly higher than other photoanodes, highlighting its notable enhancement in PEC water splitting performance.^{44,54} UV–vis absorption spectra (Figure S16a) and bandgap analysis (Figure S16b) indicate that all three samples possess comparable light absorption capacities and nearly identical bandgap energies, confirming that the performance improvement does not originate from intrinsic optical absorption differences.^{50,55}

Gas chromatography was employed to analyze the gaseous products produced during PEC water splitting (Figures S17 and 3c), with the detected H₂/O₂ molar ratio close to 2:1 (Figure S17b), confirming a complete water splitting reaction. In-Fe₂O₃ (LV) also displays an outstanding operational stability with very low dark currents, maintaining a stable performance over 50 h of chopped illumination (Figure S18). Calculation of the Faradaic efficiency (FEs) (Figure 3c) further attests to the excellent energy conversion efficiency of In-

Fe₂O₃ (LV), with values approaching 95%.^{45,56} Following FeNiOOH cocatalyst deposition, the performance of In-Fe₂O₃ (LV) is further enhanced: FeNiOOH-In-Fe₂O₃ (LV) achieves a photocurrent density of 4.32 mA cm⁻² at 1.23 V_{RHE} with an onset potential as low as 0.77 V_{RHE} (Figures 3d and S19a), representing a leading performance among comparable systems (Figure S20 and Table S2).

As shown in Figure S19b, FeNiOOH-In-Fe₂O₃ (LV) exhibits the longest average carrier lifetime of 10.18 ns, followed by In-Fe₂O₃ (LV) at 8.99 ns, and 4.60 ns for Fe₂O₃ (LV). These results indicate that, compared to Fe₂O₃ (LV), In-Fe₂O₃ (LV) achieves a significantly enhanced utilization of photogenerated holes, while FeNiOOH further boosts the hole utilization. As shown in Figure S21, compared to the pristine catalyst, the incorporation of FeNiOOH results in accelerated interfacial charge transfer (with $R_{ct} \approx 23.0 \Omega$) and an increased ABPE of 0.50%. The final photoanode also maintains excellent H₂ and O₂ production rates and a Faradaic efficiency above 95% (Figures S22 and 3e). Notably, FeNiOOH-In-Fe₂O₃ (LV) shows negligible performance decay over 50 h of chopped illumination (Figure 3f), underscoring its remarkable long-term durability and very low dark currents.

Working Mechanism. To elucidate the impact of indium incorporation on the local structure of the photoanodes, systematic analyses of the chemical environment and electronic structure were performed. X-ray photoelectron spectroscopy (XPS) was utilized to characterize the surface elemental composition and chemical states of the photoanodes. As shown in the survey spectrum (Figure S23a), the characteristic signals of Fe and O originate from the hematite phase, while the Sn signal is assigned to the FTO substrate, and the C signal is attributed to unavoidable surface contamination.³⁰ Due to the low concentration of introduced indium, no distinct indium

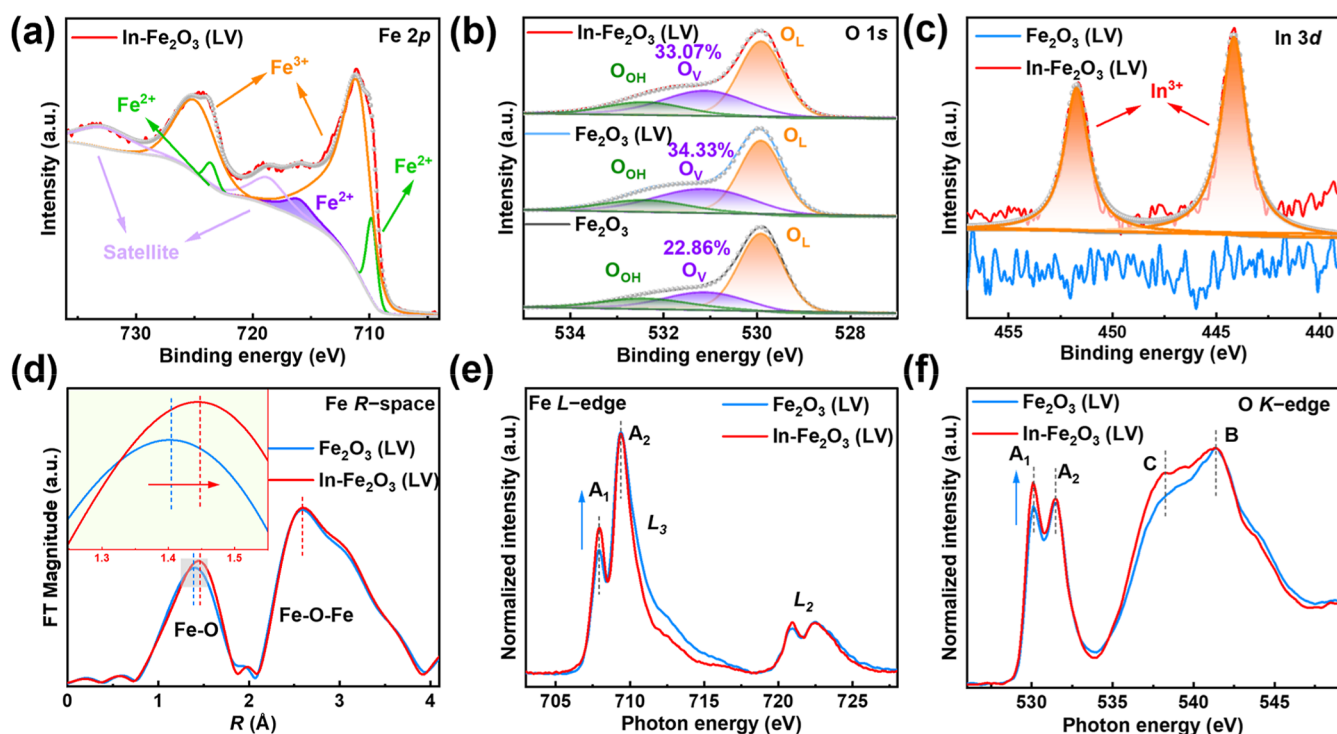


Figure 4. Chemical environment and electronic structure of In-Fe₂O₃ (LV) and Fe₂O₃ (LV). (a) Fe 2p of In-Fe₂O₃ (LV) and (b) O 1s XPS spectra of In-Fe₂O₃ (LV), Fe₂O₃ (LV) and Fe₂O₃, respectively. (c) In 3d XPS spectra of In-Fe₂O₃ (LV) and Fe₂O₃ (LV). (d) k^3 -weighted Fourier-transform spectra from EXAFS for Fe K-edge. (e) Fe L-edge and (f) O K-edge XAS spectra of In-Fe₂O₃ (LV) and Fe₂O₃ (LV), respectively.

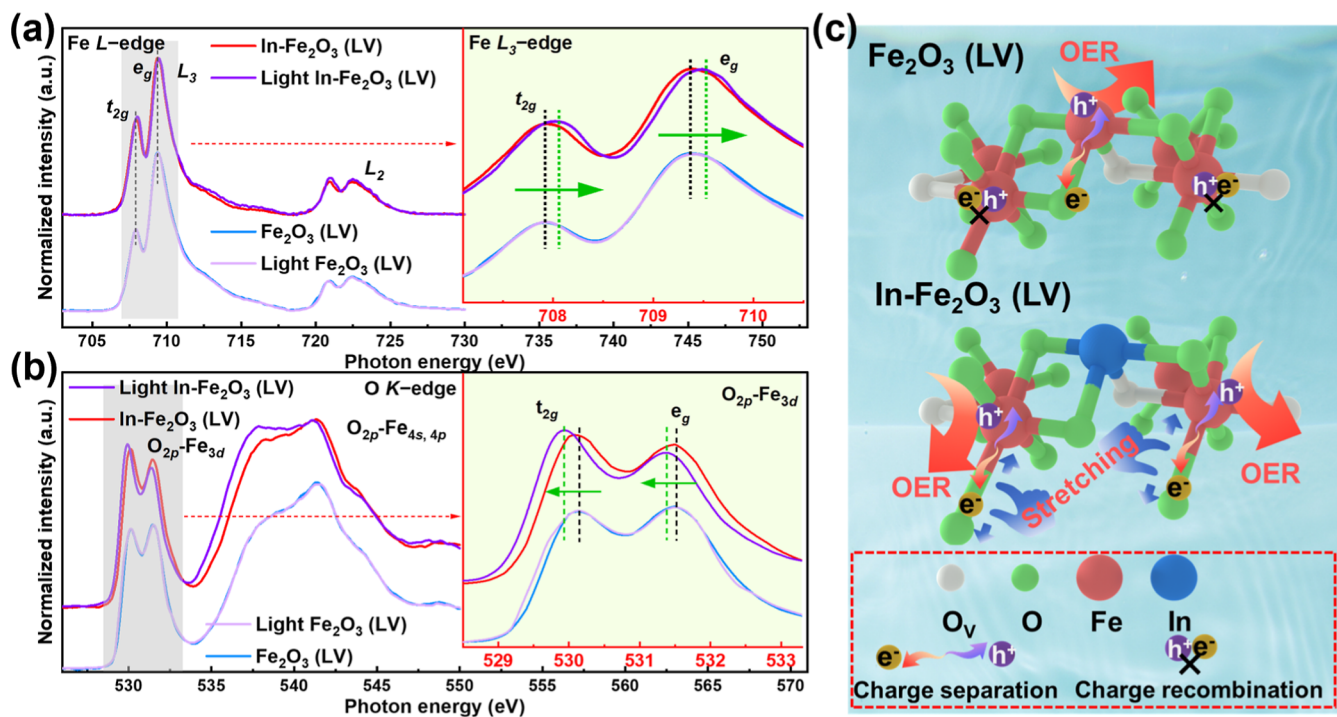


Figure 5. In situ XAS and mechanism of In-Fe₂O₃ (LV). (a) Fe L-edge and (b) O K-edge XAS spectra of In-Fe₂O₃ (LV) and Fe₂O₃ (LV) with and without light, respectively. (c) Schematic representation of the water splitting mechanism for Fe₂O₃ (LV) and In-Fe₂O₃ (LV).

signal was detected in the survey scan. Further high-resolution XPS spectra (Figures 4a–c, S23 and Table S3) comparing the Fe 2p and O 1s regions among different photoanodes reveal the pronounced Fe²⁺ peaks and oxygen vacancies (O_v) features in both Fe₂O₃ (LV) and In-Fe₂O₃ (LV), in contrast to pristine Fe₂O₃, confirming the successful introduction of oxygen

vacancies.^{13,57,58} In Figures 4a and S23, the green curve Fe²⁺ peak stands for the lower chemical state of Fe²⁺ when compared to Fe³⁺, while the purple curve Fe²⁺ peak at around 716 eV should be attributed to the oxygen vacancy induced feature as reported in the literature.^{6,26,42} As calculated in Figure 4b, the surface oxygen vacancy contents of In-Fe₂O₃

(LV) and Fe_2O_3 (LV) are 33.07 and 34.33%, respectively, significantly higher than that of pristine Fe_2O_3 (22.86%). Despite exhibiting a comparable oxygen vacancy concentration to Fe_2O_3 (LV), In- Fe_2O_3 (LV) delivers a significantly superior PEC performance, highlighting the positive effect of its local structural distortions. The electron paramagnetic resonance (EPR) data in Figure S23e also confirms the presence of oxygen vacancies. Additionally, Figures 4c and S23d provides direct evidence of successful indium doping in In- Fe_2O_3 (LV), where indium is present in the +3-oxidation state.^{59,60}

Synchrotron-based hard and soft X-ray absorption spectroscopy were employed to systematically investigate the bulk and surface electronic structure evolution of In- Fe_2O_3 (LV) photoanodes. As shown in Figure S24a, the normalized Fe *K*-edge X-ray absorption near-edge structure (XANES) spectra exhibit no discernible differences among the samples, as all display characteristic features of hematite. Thus, finer structural variations were further explored by Fourier-transforming the Fe *K*-edge EXAFS signals in *R* space (Figure 4d). Upon indium incorporation, the Fe–O coordination peak for In- Fe_2O_3 (LV) shifts to approximately 1.45 Å, slightly longer than that of Fe_2O_3 (LV) at 1.41 Å.³¹ Notably, this peak shift is only observed in In- Fe_2O_3 (LV) with oxygen vacancies modification (along with heterophase), while no similar change is found in In- Fe_2O_3 samples without oxygen vacancies (Figure S24b). It is also consistent with the limited PEC performance enhancement of In- Fe_2O_3 as shown in Figure S24c.

Figure 4e,f show the Fe *L*-edge and O *K*-edge X-ray absorption spectra, respectively, with all samples displaying the characteristic features of Fe_2O_3 . The L_3 and L_2 -edges in Figure 4e correspond to Fe 2*p* to unoccupied 3*d* transitions, split into A_1 and A_2 peaks (t_{2g} and e_g) due to crystal field effects.⁶¹ In Figure 4f, two distinct pre-edge peaks (A_1 and A_2) at around 530 eV are attributed to O 1*s* to O 2*p*-Fe 3*d* hybridized states, while the main peak B (~540 eV) arises from O 2*p* and Fe 4*s**p* hybridization.⁶² With indium incorporation, an enhanced spectral feature at around 536 eV (peak C) is observed, which can be ascribed to O 2*p*-In 5*p* hybridization.⁶³ These electronic structure analyses at the Fe *L*-edge and O *K*-edge demonstrate that indium is effectively incorporated without disrupting the characteristic Fe_2O_3 structure. Importantly, compared to Fe_2O_3 (LV), the In- Fe_2O_3 (LV) samples exhibit a pronounced increase in the A_1 peak intensity at both Fe *L*-edge and O *K*-edge, indicating enhanced O 2*p*-Fe 3*d* hybridized states, likely associated with Fe–O bond elongation.^{64,65} This increased hybridization is expected to facilitate interfacial charge transfer.⁶⁵

To further explore the intrinsic mechanism of In- Fe_2O_3 (LV) for efficient PEC water splitting—specifically the influence of local structural modifications on its performance—in situ X-ray absorption spectroscopy (XAS) was performed under illumination conditions (Figure 5a,b; right panels show local magnifications). As shown in Figure 5a, a pronounced shift of the Fe *L*-edge toward higher energy is observed for In- Fe_2O_3 (LV) under light irradiation, indicating the transfer of photogenerated holes to Fe^{3+} sites and the formation of Fe^{4+} species.²² This phenomenon can be attributed to the enhanced O 2*p*-Fe 3*d* hybridization induced by local structural distortion, which facilitates interfacial charge transfer.^{64,65} Under illumination, photogenerated holes exhibit enhanced transfer efficiency to Fe sites, thereby enabling more effective participation in the oxygen evolution reaction.

Simultaneously, the A_1 and A_2 peaks of the O *K*-edge in Figure 5b exhibit a clear shift to lower energies, directly reflecting the migration of photogenerated electrons into lattice oxygen on the hematite surface and resulting in the observed energy decrease.^{22,66} In contrast, Fe_2O_3 (LV) samples without local structural distortion show no such peak position or shape changes in the Fe *L*-edge or O *K*-edge XAS spectra under illumination, which can be ascribed to severe surface charge recombination. Overall, these in situ XAS results demonstrate that locally distorted structures enhance O 2*p*-Fe 3*d* hybridization, thereby promoting efficient interfacial charge transfer. Consequently, In- Fe_2O_3 (LV) exhibits improved separation of photogenerated electron–hole pairs, accelerating the oxygen evolution reaction and lowering the onset potential.

Based on the combined results from ex situ and in situ XAS, the working mechanism of the In- Fe_2O_3 (LV) photoanode is illustrated in Figure 5c. The introduction of oxygen vacancies (along with heterophase) enhances the electrical conductivity and carrier density of the photoanode; however, it also generates numerous charge recombination centers within both the bulk and surface regions, impeding efficient charge transport and separation (top panel). Notably, the abundant oxygen vacancies with heterophase provide a buffer for Indium incorporation, thereby mitigating the formation of recombination centers caused by structural strain. Indium doping further elongates the Fe–O bonds, inducing local structural distortions and altering the O 2*p*-Fe 3*d* orbital hybridization. This facilitates the migration of photogenerated charges, enabling photoinduced holes to transfer more readily to Fe^{3+} sites and form highly active Fe^{4+} species. These synergistic effects substantially improve surface charge separation efficiency, result in a lower onset potential, and ultimately enhance the photoelectrochemical water splitting performance.

CONCLUSIONS

In conclusion, this work illustrates that the collaborative modification of hematite with indium and oxygen vacancies (along with heterophase) efficiently triggers local structural distortions, resulting in the development of high-performance In- Fe_2O_3 (LV) photoanode. Static XAS results revealed that Fe–O bond stretching induces local structural distortion in the photoanode, enhancing O 2*p*-Fe 3*d* orbital hybridization. In situ XAS observations captured transient electronic structure changes at Fe sites, elucidating their structure–activity relationship with the stretching of Fe–O bond. The enhanced O 2*p*-Fe 3*d* orbital hybridization accelerates photogenerated charge carrier transfer, promoting hole migration to Fe^{3+} sites and generating high-valence Fe^{4+} , which significantly improves OER kinetics and reduces the onset potential. As a result, the oxygen evolution reaction kinetics are notably enhanced, and the onset potential is decreased. Accordingly, the In- Fe_2O_3 (LV) photoanode attains a photocurrent density of 3.66 mA cm^{-2} at 1.23 V_{RHE} , showing a 4.3-fold increase relative to pristine Fe_2O_3 . It features an onset potential of 0.86 V_{RHE} , which is 130 mV lower than that of Fe_2O_3 (LV), and maintains excellent operational stability. With the addition of a FeNiOOH cocatalyst, the FeNiOOH–In- Fe_2O_3 (LV) photoanode shows a further improved photocurrent density of 4.32 mA cm^{-2} and a decreased onset potential of 0.77 V_{RHE} , emphasizing its outstanding potential for practical use.

EXPERIMENTAL SECTION

Material Preparation. β -FeOOH/FTO and In- β -FeOOH/FTO were obtained by a conventional hydrothermal method. As shown in Figures 1a, S1 and S2, FTO conductive glass (30 mm \times 50 mm) was first ultrasonically cleaned successively with acetone, ethanol, and deionized water for 15 min each. The precursor solution (0.06 M FeCl₃·6H₂O and 0.06 M NaNO₃) and FTO conductive glass (with the conductive side facing up) were then placed in a 100 mL stainless steel autoclave for hydrothermal reaction at 95 °C for 240 min to obtain β -FeOOH/FTO.^{26,27} For the preparation of In- β -FeOOH/FTO, different concentrations of InCl₃ solution (30, 60, 90, 120 mg mL⁻¹) were added into the precursor solution.

Fe₂O₃ and In-Fe₂O₃ photoanodes were obtained by a conventional annealing method.^{26,27} As shown in Figures S1 and S2, the dried β -FeOOH/FTO and In- β -FeOOH/FTO were annealed in a muffle furnace at 550 °C for 120 min and then at 750 °C for 15 min, resulting in the formation of α -Fe₂O₃ (denoted as Fe₂O₃) and In-doped α -Fe₂O₃ (denoted as In-Fe₂O₃) photoanodes.

Fe₂O₃ (LV) and In-Fe₂O₃ (LV) photoanodes were prepared by a high-temperature and variable-pressure annealing method.^{26,27} As shown in Figures 1a and S1, the dried β -FeOOH/FTO and In- β -FeOOH/FTO were placed in a tube furnace and annealed under higher vacuum at 550 °C for 120 min, followed by annealing in air under relatively lower vacuum at 750 °C for 15 min, ultimately yielding oxygen vacancy-modified α -Fe₂O₃ (denoted as Fe₂O₃ (LV)) and In/oxygen vacancy comodified α -Fe₂O₃ (denoted as In-Fe₂O₃ (LV)) photoanodes.

The FeNiOOH–In-Fe₂O₃ (LV) composite was fabricated via the photoelectrodeposition technique. The electrolyte solution was prepared by dissolving 5 mM FeCl₃·6H₂O, 3 mM NiCl₂·6H₂O, 5 mM NaF, and 0.1 mM KCl in 100 mL of deionized water. The FeNiOOH–In-Fe₂O₃ (LV) photoanode was deposited using cyclic voltammetry. Specifically, the deposition potential range was set at –0.49 to 0.41 V versus Ag/AgCl, the scan rate was maintained at 0.2 V s⁻¹, and the cyclic process was performed twice.

Characterization. The microstructure and morphology were characterized by SEM (ZEISS G500) and TEM (Talos 200X). Crystal structure analysis and surface chemical states were performed by XRD (PANalytical, Zmpyran) and XPS (Kratos AXIS UltraDLD). Optical absorption properties were evaluated using a UV–vis–NIR spectrophotometer (PE950). The evolved gases were collected and analyzed by a gas chromatograph (GC-7900, Techcomp, Shanghai, China) to determine the composition and yield. X-ray absorption spectroscopy (XAS) measurements were conducted at NSRL (MCD-A and MCD-B) and SSRF (20U).

ASSOCIATED CONTENT

Supporting Information

The Supporting Information is available free of charge at <https://pubs.acs.org/doi/10.1021/acscatal.5c04809>.

Additional XRD spectra, SEM images, TEM images, XPS analyses, XAS spectrum, electrochemical measurements and two tables (PDF)

AUTHOR INFORMATION

Corresponding Author

Jun Zhong – Institute of Functional Nano and Soft Materials Laboratory (FUNSOM), Jiangsu Key Laboratory of Advanced Negative Carbon Technologies, Soochow University, Suzhou 215123, China; orcid.org/0000-0002-8768-1843; Email: jzhong@suda.edu.cn

Authors

Cheng Lu – Institute of Functional Nano and Soft Materials Laboratory (FUNSOM), Jiangsu Key Laboratory of Advanced Negative Carbon Technologies, Soochow University, Suzhou 215123, China

Zihou Jiang – Institute of Functional Nano and Soft Materials Laboratory (FUNSOM), Jiangsu Key Laboratory of Advanced Negative Carbon Technologies, Soochow University, Suzhou 215123, China

Jiabin Xu – Department of Chemistry and Soochow-Western Centre for Synchrotron Radiation Research, University of Western Ontario, London, Ontario N6A 5B7, Canada; orcid.org/0000-0002-9693-2261

Shuo Li – State Key Laboratory of Radiation Medicine and Protection, School for Radiological and Interdisciplinary Sciences (RAD-X) and Collaborative Innovation Center of Radiation Medicine of Jiangsu Higher Education Institutions, Soochow University, Suzhou 215123, China

Yong Feng – Institute of Functional Nano and Soft Materials Laboratory (FUNSOM), Jiangsu Key Laboratory of Advanced Negative Carbon Technologies, Soochow University, Suzhou 215123, China; orcid.org/0009-0002-5988-9580

Bai Xu – Institute of Functional Nano and Soft Materials Laboratory (FUNSOM), Jiangsu Key Laboratory of Advanced Negative Carbon Technologies, Soochow University, Suzhou 215123, China

Gongcheng Liu – Institute of Functional Nano and Soft Materials Laboratory (FUNSOM), Jiangsu Key Laboratory of Advanced Negative Carbon Technologies, Soochow University, Suzhou 215123, China

Ye Zhu – Institute of Functional Nano and Soft Materials Laboratory (FUNSOM), Jiangsu Key Laboratory of Advanced Negative Carbon Technologies, Soochow University, Suzhou 215123, China

Kun Feng – Institute of Functional Nano and Soft Materials Laboratory (FUNSOM), Jiangsu Key Laboratory of Advanced Negative Carbon Technologies, Soochow University, Suzhou 215123, China

Complete contact information is available at: <https://pubs.acs.org/doi/10.1021/acscatal.5c04809>

Author Contributions

^{||}C.L. and Z.J. contributed equally.

Notes

The authors declare no competing financial interest.

ACKNOWLEDGMENTS

We appreciate the support from NSRL (<https://cstr.cn/31131.02.HLS.XMCD.a> and <https://cstr.cn/31131.02.HLS.XMCD.b>) and SSRF (<https://cstr.cn/31124.02.SSRF.BL20U1>) for the XAS experiments. This research is funded by the National Key R&D Program of China (2020YFA0406103), the National Natural Science Foundation of China (U1932211), the

Collaborative Innovation Center of Suzhou Nano Science & Technology, the Priority Academic Program Development of Jiangsu Higher Education Institutions (PAPD), Jiangsu Key Laboratory for Carbon-Based Functional Materials and Devices (ZZ2201) and the 111 Project.

REFERENCES

- (1) Hyun, J.; Kim, H.-T. Powering the hydrogen future: current status and challenges of anion exchange membrane fuel cells. *Energy Environ. Sci.* **2023**, *16*, 5633–5662.
- (2) Wang, J.; Liu, K.; Liao, W.; Kang, Y.; Xiao, H.; Chen, Y.; Wang, Q.; Luo, T.; Chen, J.; Li, H.; Chan, T.-S.; Chen, S.; Pensa, E.; Chai, L.; Liu, F.; Jiang, L.; Liu, C.; Fu, J.; Cortés, E.; Liu, M. Metal vacancies in semiconductor oxides enhance hole mobility for efficient photoelectrochemical water splitting. *Nat. Catal.* **2025**, *8*, 229–238.
- (3) Wang, C.; Schechter, A.; Feng, L. Iridium-based catalysts for oxygen evolution reaction in acidic media: Mechanism, catalytic promotion effects and recent progress. *Nano Res. Energy* **2023**, *2*, No. e9120056.
- (4) Su, Z.; Huang, Q.; Guo, Q.; Hoseini, S. J.; Zheng, F.; Chen, W. Metal-organic framework and carbon hybrid nanostructures: Fabrication strategies and electrocatalytic application for the water splitting and oxygen reduction reaction. *Nano Res. Energy* **2023**, *2*, No. e9120078.
- (5) Deng, J.; Zhang, Q.; Lv, X.; Zhang, D.; Xu, H.; Ma, D.; Zhong, J. Understanding photoelectrochemical water oxidation with X-ray absorption spectroscopy. *ACS Energy Lett.* **2020**, *5*, 975–993.
- (6) Yoon, K.-Y.; Park, J.; Jung, M.; Ji, S.-G.; Lee, H.; Seo, J. H.; Kwak, M.-J.; Il Seok, S.; Lee, J. H.; Jang, J.-H. NiFeO_x decorated Ge-hematite/perovskite for an efficient water splitting system. *Nat. Commun.* **2021**, *12*, 4309.
- (7) Li, C.; Luo, Z.; Wang, T.; Gong, J. Surface, bulk, and interface: Rational design of hematite architecture toward efficient photoelectrochemical water splitting. *Adv. Mater.* **2018**, *30*, 1707502.
- (8) Zhang, H.; Li, D.; Byun, W. J.; Wang, X.; Shin, T. J.; Jeong, H. Y.; Han, H.; Li, C.; Lee, J. S. Gradient tantalum-doped hematite homojunction photoanode improves both photocurrents and turn-on voltage for solar water splitting. *Nat. Commun.* **2020**, *11*, 4622.
- (9) Jiang, S.; Ding, L.; Liu, D.; Wang, G.; Tao, R.; Chu, Z.; Fan, X.; Guan, J. Dual internal electric field synergistic interface and surface modification enhance photoelectrochemical performance of hematite photoanodes. *J. Mater. Chem. A* **2025**, *13*, 12500.
- (10) Uemura, Y.; Ismail, A. S. M.; Park, S. H.; Kwon, S.; Kim, M.; Elnaggar, H.; Frati, F.; Wadati, H.; Hirata, Y.; Zhang, Y.; Yamagami, K.; Yamamoto, S.; Matsuda, I.; Halisdemir, U.; Koster, G.; Milne, C.; Ammann, M.; Weckhuysen, B. M.; de Groot, F. M. F. Hole dynamics in photoexcited hematite studied with femtosecond oxygen K-edge X-ray absorption spectroscopy. *J. Phys. Chem. Lett.* **2022**, *13*, 4207.
- (11) Liu, H.; Fan, X.; Li, Y.; Guo, H.; Jiang, W.; Liu, G. Hematite-based photoanodes for photoelectrochemical water splitting: Performance, understanding, and possibilities. *J. Environ. Chem. Eng.* **2023**, *11*, 109224.
- (12) Yi, S.-S.; Yan, J.-M.; Jiang, Q. Carbon quantum dot sensitized integrated Fe₂O₃@g-C₃N₄ core-shell nanoarray photoanode towards highly efficient water oxidation. *J. Mater. Chem. A* **2018**, *6*, 9839–9845.
- (13) Zhang, Z.; Karimata, I.; Nagashima, H.; Muto, S.; Ohara, K.; Sugimoto, K.; Tachikawa, T. Interfacial oxygen vacancies yielding long-lived holes in hematite mesocrystal-based photoanodes. *Nat. Commun.* **2019**, *10*, 4832.
- (14) Yoon, K.-Y.; Park, J.; Lee, H.; Seo, J. H.; Kwak, M.-J.; Lee, J. H.; Jang, J.-H. Unveiling the role of the Ti dopant and viable Si doping of hematite for practically efficient solar water splitting. *ACS Catal.* **2022**, *12*, 5112–5122.
- (15) Singh, A. P.; Tossi, C.; Tittonen, I.; Hellman, A.; Wickman, B. Synergies of co-doping in ultra-thin hematite photoanodes for solar water oxidation: In and Ti as representative case. *RSC Adv.* **2020**, *10*, 33307–33316.
- (16) Quang, N. D.; Van, P. C.; Le, D. D.; Majumder, S.; Chinh, N. D.; Jeong, J.-R.; Kim, C.; Kim, D. Fluorine-surface-modified tin-doped hematite nanorod array photoelectrodes with enhanced water oxidation activity. *Appl. Surf. Sci.* **2021**, *558*, 149898.
- (17) Chen, D.; Liu, Z. Dual-axial gradient doping (Zr and Sn) on hematite for promoting charge separation in photoelectrochemical water splitting. *ChemSusChem* **2018**, *11*, 3438–3448.
- (18) Zhou, Z.; Wu, S.; Qin, L.; Li, L.; Li, L.; Li, X. Modulating oxygen vacancies in Sn-doped hematite film grown on silicon microwires for photoelectrochemical water oxidation. *J. Mater. Chem. A* **2018**, *6*, 15593–15602.
- (19) Rani, B. J.; Ravi, G.; Yuvakkumar, R.; Ravichandran, S.; Ameen, F.; AlNadhary, S. Sn doped α -Fe₂O₃ (Sn = 0,10,20,30 wt%) photoanodes for photoelectrochemical water splitting applications. *Renewable Energy* **2019**, *133*, 566–574.
- (20) Ruoko, T. P.; Hiltunen, A.; Iivonen, T.; Ulkuniemi, R.; Lahtonen, K.; Ali-Loytty, H.; Mizohata, K.; Valden, M.; Leskela, M.; Tkachenko, N. V. Charge carrier dynamics in tantalum oxide overlayers and tantalum doped hematite photoanodes. *J. Mater. Chem. A* **2019**, *7*, 3206–3215.
- (21) Jiao, T.; Lu, C.; Zhang, D.; Feng, K.; Wang, S.; Kang, Z.; Zhong, J. Bi-functional Fe₂ZrO₅ modified hematite photoanode for efficient solar water splitting. *Appl. Catal., B* **2020**, *269*, 118768.
- (22) Li, C.; Lu, C.; Zhu, Y.; Li, S.; Feng, Y.; Yang, Y.; Xu, B.; Feng, K.; Zhong, J. In-situ electron capture by surface Co-Ci to facilitate the solar water splitting of Fe₂O₃. *Chem. Eng. J.* **2024**, *486*, 150120.
- (23) Sivula, K.; Zboril, R.; Formal, F. L.; Robert, R.; Weidenkaff, A.; Tucek, J.; Frydrych, J.; Grätzel, M. Photoelectrochemical water splitting with mesoporous hematite prepared by a solution-based colloidal approach. *J. Am. Chem. Soc.* **2010**, *132*, 7436–7444.
- (24) Pu, A.; Deng, J.; Li, M.; Gao, J.; Zhang, H.; Hao, Y.; Zhong, J.; Sun, X. Coupling Ti-doping and oxygen vacancies in hematite nanostructures for solar water oxidation with high efficiency. *J. Mater. Chem. A* **2014**, *2*, 2491–2497.
- (25) Gao, R. T.; Zhang, J.; Nakajima, T.; He, J.; Liu, X.; Zhang, X.; Wang, L.; Wu, L. Single-atomic-site platinum steers photogenerated charge carrier lifetime of hematite nanoflakes for photoelectrochemical water splitting. *Nat. Commun.* **2023**, *14*, 2640.
- (26) Park, J.; Yoon, K.-Y.; Ghule, B. G.; Kim, H.; Jang, J.-H. Morphology-engineered hematite photoanode for photoelectrochemical water splitting. *ACS Energy Lett.* **2024**, *9*, 3169–3176.
- (27) Liu, S.; Wu, L.; Tang, D.; Xue, J.; Dang, K.; He, H.; Bai, S.; Ji, H.; Chen, C.; Zhang, Y.; Zhao, J. Transition from sequential to concerted proton-coupled electron transfer of water oxidation on semiconductor photoanodes. *J. Am. Chem. Soc.* **2023**, *145*, 23849–23858.
- (28) Mesa, C. A.; Francas, L.; Yang, K. R.; Garrido-Barros, P.; Pastor, E.; Ma, Y.; Kafizas, A.; Rosser, T. E.; Mayer, M. T.; Reisner, E.; Grätzel, M.; Batista, V. S.; Durrant, J. R. Multihole water oxidation catalysis on hematite photoanodes revealed by operando spectroelectrochemistry and DFT. *Nat. Chem.* **2020**, *12*, 82–89.
- (29) Xu, S.; Yang, J.; Su, P.; Wang, Q.; Yang, X.; Zhou, Z.; Li, Y. Identifying key intermediates for the oxygen evolution reaction on hematite using ab-initio molecular dynamics. *Nat. Commun.* **2024**, *15*, 10411.
- (30) Lu, C.; Zhang, D.; Wu, Z.; Zhao, X.; Feng, K.; Zhang, G.; Wang, S.; Kang, Z.; Zhong, J. Hetero phase modulated hematite photoanodes for practical solar water splitting. *Appl. Catal., B* **2023**, *331*, 122695.
- (31) Lu, C.; Feng, K.; Li, C.; Xu, J.; Li, S.; Feng, Y.; Zhu, Y.; Wang, S.; Zhong, J. Distorted Ge-O-Fe microstructure as an active unit in hematite to accelerate solar water splitting. *ACS Materials Lett.* **2024**, *6*, 1571–1580.
- (32) Fouemina, J. C. N.; Li, G.; She, X.; Yan, D.; Lv, X.; Nie, K.; Deng, J.; Xu, H. Surface self-transforming FeTi-LDH Overlayer in Fe₂O₃/Fe₂TiO₅ photoanode for improved water oxidation. *Small* **2023**, *19*, 2301114.
- (33) Quang, N. D.; Hu, W.; Chang, H. S.; Van, P. C.; Viet, D. D.; Jeong, J.-R.; Seo, D. B.; Kim, E. T.; Kim, C.; Kim, D. Fe₂O₃

hierarchical tubular structure decorated with cobalt phosphide (CoP) nanoparticles for efficient photoelectrochemical water splitting. *Chem. Eng. J.* **2021**, *417*, 129278.

(34) Wang, C.; Geng, Q.; Fan, L.; Li, J.-X.; Ma, L.; Li, C. Phase engineering oriented defect-rich amorphous/crystalline RuO₂ nanoporous particles for boosting oxygen evolution reaction in acid media. *Nano Res. Energy* **2023**, *2*, No. e9120070.

(35) Li, Y.; Zhang, N.; Liu, C.; Zhang, Y.; Xu, X.; Wang, W.; Feng, J.; Li, Z.; Zou, Z. Metastable-phase β -Fe₂O₃ photoanodes for solar water splitting with durability exceeding 100 h. *Chin. J. Catal.* **2021**, *42*, 1992–1998.

(36) Guo, F.; Bai, J.; Gao, R.-T.; Su, K.; Yang, Y.; Liu, X.; Wu, L.; Wang, L. Enhanced charge transfer via heterogeneous doping promotes hematite photoelectrodes for efficient solar H₂O₂ synthesis. *ACS Catal.* **2024**, *14*, 4369–4378.

(37) Koh, T. S.; Anushkaran, P.; Chae, W.-S.; Lee, H. H.; Choi, S. H.; Jang, J. S. Gradient Si- and Ti-doped Fe₂O₃ hierarchical homojunction photoanode for efficient solar water splitting: Effect of facile microwave-assisted growth of Si-FeOOH on Ti-FeOOH nanocorals. *J. Energy Chem.* **2023**, *77*, 27–37.

(38) Luo, Z.; Wang, T.; Zhang, J.; Li, C.; Li, H.; Gong, J. Dendritic hematite nanorod photoanode modified with a conformal titanium dioxide interlayer for effective charge collection. *Angew. Chem., Int. Ed.* **2017**, *56*, 12878–12882.

(39) Sivula, K. Mott-Schottky analysis of photoelectrodes: Sanity checks are needed. *ACS Energy Lett.* **2021**, *6*, 2549–2551.

(40) Kang, J.; Ghule, B. G.; Gyeong, S. G.; Ha, S.-J.; Jang, J.-H. Alleviating charge recombination caused by unfavorable interaction of P and Sn in hematite for photoelectrochemical water oxidation. *ACS Catal.* **2024**, *14*, 10355–10364.

(41) Chaule, S.; Kang, J.; Ghule, B. G.; Kim, H.; Jang, J.-H. An approach to enhance PEC water splitting performance through Al:Ti codoping in hematite (α -Fe₂O₃) photoanode: The effect of Al³⁺ as a codopant. *ACS Materials Lett.* **2024**, *6*, 2897–2904.

(42) Xie, H.; Song, Y.; Jiao, Y.; Gao, L.; Shi, S.; Wang, C.; Hou, J. Engineering surface passivation and hole transport layer on hematite photoanodes enabling robust photoelectrocatalytic water oxidation. *ACS Nano* **2024**, *18*, 5712–5722.

(43) Jiang, S.; Cheng, M.; Liu, D.; Tao, R.; Chu, Z.; Fan, X.; Guan, J. FeS as hole transport pathway regulating charge transfer for efficient photoelectrochemical water splitting of hematite photoanodes. *Chem. Eng. J.* **2025**, *504*, 158993.

(44) Li, W.; Guo, H.; Xu, C.; Tang, C.; Lee, J. S.; Zhang, H. Hole storage overlayer of amorphous hafnium oxide for boosting hematite-based solar water splitting. *Appl. Catal., B* **2024**, *342*, 123465.

(45) Xu, C.; Wang, H.; Guo, H.; Liang, K.; Zhang, Y.; Li, W.; Chen, J.; Lee, J. S.; Zhang, H. Parallel multi-stacked photoanodes of Sb-doped p-n homojunction hematite with near-theoretical solar conversion efficiency. *Nat. Commun.* **2024**, *15*, 9712.

(46) Xu, C.; Wang, H.; Liang, K.; Zhang, Y.; Li, W.; Zhang, H. Inducing hollow and porous hematite nanorod photoanodes by rare earth and transition metal doping for enhanced solar water splitting. *J. Mater. Chem. A* **2024**, *12*, 11831–11840.

(47) Liu, Y.; Le Formal, F.; Boudoire, F.; Guijarro, N. Hematite photoanodes for solar water splitting: A detailed spectroelectrochemical analysis on the pH-dependent performance. *ACS Appl. Energy Mater.* **2019**, *2*, 6825–6833.

(48) Shi, X.; Zhang, K.; Park, J. H. Understanding the positive effects of (Co–Pi) co-catalyst modification in inverse-opal structured α -Fe₂O₃-based photoelectrochemical cells. *Int. J. Hydrogen Energy* **2013**, *38*, 12725–12732.

(49) Wu, F.; Xie, J.; You, Y.; Zhao, Z.; Wang, L.; Chen, X.; Yang, P.; Huang, Y. Cobalt metal-organic framework ultrathin cocatalyst overlayer for improved photoelectrochemical activity of Ti-doped hematite. *ACS Appl. Energy Mater.* **2020**, *3*, 4867–4876.

(50) Deng, J.; Li, G.; Yan, D.; Zhang, W.; Feng, K.; Nie, K.; Liu, C.; Lv, X.; Zhong, J. Programmable wet-interfacial joule heating to rapidly synthesize metastable protohematite photoanodes: Metal and lattice

oxygen dual sites for improving water oxidation. *ACS Catal.* **2024**, *14*, 10635–10647.

(51) Li, G.; Jang, H.; Liu, S.; Li, Z.; Kim, M. G.; Qin, Q.; Liu, X.; Cho, J. The synergistic effect of Hf–O–Ru bonds and oxygen vacancies in Ru/HfO₂ for enhanced hydrogen evolution. *Nat. Commun.* **2022**, *13*, 1270.

(52) Xiao, Y.; Fu, J.; Pihosh, Y.; Karmakar, K.; Zhang, B.; Domen, K.; Li, Y. Interface engineering for photoelectrochemical oxygen evolution reaction. *Chem. Soc. Rev.* **2025**, *54*, 1268–1317.

(53) Yang, T.; Chen, Z. W.; Yue, X. Z.; Liu, Q. C.; Yi, S. S.; Zhu, Y. F. Interfacial charge transfer bridge prolongs carrier recombination lifetimes of CoFe metal-thiolate framework/hematite photoanode for water oxidation. *Adv. Funct. Mater.* **2024**, *34*, 2313767.

(54) Ye, R.-K.; Sun, S.-S.; He, L.-Q.; Yang, S.-R.; Liu, X.-Q.; Li, M.-D.; Fang, P.-P.; Hu, J.-Q. Surface engineering of hematite nanorods by 2D Ti₃C₂-MXene: Suppressing the electron-hole recombination for enhanced photoelectrochemical performance. *Appl. Catal., B* **2021**, *291*, 120107.

(55) Yoon, K.-Y.; Ahn, H.-J.; Kwak, M.-J.; Kim, S.-I.; Park, J.; Jang, J.-H. A selectively decorated Ti-FeOOH co-catalyst for a highly efficient porous hematite-based water splitting system. *J. Mater. Chem. A* **2016**, *4*, 18730–18736.

(56) Li, C.; Xiao, J.; Jia, X.; Zhao, Q.; Du, B.; Wang, B. Unveiling the influence of lower-valence Ni in hydroxide Co-catalyst and attaining efficient photoanodes with FeOOH holes transfer layer for photoelectrochemical water splitting. *Adv. Funct. Mater.* **2024**, *35*, 2406999.

(57) Xu, Y.; Zhang, H.; Gong, D.; Chen, Y.; Xu, S.; Qiu, P. Solar water splitting with nanostructured hematite: the role of oxygen vacancy. *J. Mater. Sci.* **2022**, *57*, 19716–19729.

(58) Wang, Z. L.; Mao, X.; Chen, P.; Xiao, M.; Monny, S. A.; Wang, S. C.; Konarova, M.; Du, A. J.; Wang, L. Z. Understanding the roles of oxygen vacancies in hematite-based photoelectrochemical processes. *Angew. Chem., Int. Ed.* **2019**, *58*, 1030–1034.

(59) Wissink, T.; Rollier, F. A.; Muravev, V.; Heinrichs, J. M. J. J.; van de Poll, R. C. J.; Zhu, J.; Anastasiadou, D.; Kosinov, N.; Figueiredo, M. C.; Hensen, E. J. M. Ce Promotion of In₂O₃ for electrochemical reduction of CO₂ to formate. *ACS Catal.* **2024**, *14*, 16589–16604.

(60) Meng, J.; Liang, M.; Mu, J.; Miao, Z.; Huang, H.; Qi, R.; Diao, L.; Zhuo, S.; Zhou, J. Regulating p-orbital electronic configuration of In₂O₃ by thickness-controlled carbon layer for efficient electrocatalytic CO₂ reduction to HCOOH. *Appl. Catal., B* **2025**, *361*, 124596.

(61) Shen, S.; Zhou, J.; Dong, C. L.; Hu, Y.; Tseng, E. N.; Guo, P.; Guo, L.; Mao, S. S. Surface engineered doping of hematite nanorod arrays for improved photoelectrochemical water splitting. *Sci. Rep.* **2014**, *4*, 6627.

(62) Ye, Y.; Thorne, J. E.; Wu, C. H.; Liu, Y. S.; Du, C.; Jang, J. W.; Liu, E.; Wang, D.; Guo, J. Strong O 2p–Fe 3d hybridization observed in solution-grown hematite films by soft X-ray spectroscopies. *J. Phys. Chem. B* **2018**, *122*, 927–932.

(63) Frati, F.; Hunault, M.; de Groot, F. M. F. Oxygen K-edge X-ray absorption spectra. *Chem. Rev.* **2020**, *120*, 4056–4110.

(64) He, F.; Liu, Y.; Yang, X.; Chen, Y.; Yang, C.-C.; Dong, C.-L.; He, Q.; Yang, B.; Li, Z.; Kuang, Y.; Lei, L.; Dai, L.; Hou, Y. Accelerating oxygen electrocatalysis kinetics on metal-organic frameworks via bond length optimization. *Nano-Micro Lett.* **2024**, *16*, 175.

(65) Sun, Y.; Xie, Y.; Chen, X.; Wu, J.; Liu, P.; Wang, X.; Tian, Z.; Zheng, W.; Jiang, Z.; Kang, Z.; Zhang, Y. Updating the sub-nanometric cognition of reconstructed oxyhydroxide active phase for water oxidation. *Nat. Commun.* **2025**, *16*, 3073.

(66) Zhu, Y.; Lu, C.; Feng, Y.; Xu, J.; Li, S.; Xu, B.; Zhao, H.; Feng, K.; Zhong, J. In-situ observation of electron injection to surface carbon layer from illuminated hematite for efficient solar water oxidation. *J. Mater. Sci. Technol.* **2025**, *239*, 172–179.